IJMF, Iranian Journal of Materials Forming, Vol.5, No. 2, pp 54-71
Printed in The Islamic Republic of Iran, 2018

Determination of the Residual Stress for Single and Double Autofrettage of Thick-walled FG Cylinders Subjected to Dynamic Loading

S.H. Razi Mousavi*, M. Mahzoon, M.H. Kadivar

School of Mechanical Engineering, Shiraz university, Shiraz, Iran.

Abstract: In the present article, a numerical procedure is developed for dynamic analysis of single and double autofrettage of thick–walled Functionally Graded (FG) cylinders under transient loading. The governing differential equations are discretized and presented in explicit Lagrangian formalism. The explicit transient solution to discrete equations is obtained on the meshed region, and results for stress and strain distribution for relevant problems under inner and/or outer boundary conditions are established.

The autofrettage behavior is subsequently analyzed through the application of time dependent pressure to boundary regions of the axisymmetric domain. Dynamic results, in particular in transient loading, are different in comparison with static ones due to the presence of plastic deformation and wave propagation. The residual stress resulting from internal pressure changes the structural load bearing capacity of the cylinder, in so far as the tensile stress of the outer layers might reduce, while the compressive stress of the inner layers might increase. For functionally graded materials whose material properties change continuously, dynamic analysis yields results which are entirely different as compared with their static counterparts due to the change in the wavelength and acoustic impedance. In the static analysis, the dimensionless forms of equations can be developed from the onset, while in the dynamic analysis the physical dimensions and material properties gain importance due to the inherent properties of the stress waves. Residual stresses in the inner and outer parts of the cylinder are also studied for various volume fractions of FG material under single or double autofrettage.

Keywords: FG cylinder, Double autofrettage, Dynamic simulation, Time dependent loading, Residual stress.

1. Introduction

There have been numerous investigations related to the analysis of residual stresses and deformation in thick-walled cylinders subjected to autofrettage. Franklin and Morrison [1] investigated the behavior of homogeneous thick cylinders subjected to one or two cycles of internal pressure. They calculated the stresses throughout the material of these cylinders at any stage in the process. Chen [2] has reported a method for stress and deformation analysis based on a new theoretical model. This new model is a close representation of the actual loading/unloading behavior in a high strength steel. The strain-hardening effect is taken into account with different parameters used for loading and unloading processes.

The formulas for calculating stresses, strains, and displacements are given, and new results for residual stresses in autofrettaged high pressure vessels are presented by Stacey and Webster [3]. They compared analytical and numerical estimates with experimental measurements using Sachs boring and neutron diffraction methods. The significance of the choice of yield criterion, the Bauschinger effect and work-hardening on the predicted residual hoop stress distribution was also examined. Rees [4] showed that the bending of a thick-walled cylinder to a given radius involves an elastic–plastic deformation that results in a residual, axial stress distribution. Parker [5] investigated autofrettaged mono-block cylinders by reviewing

Received by the editors July 31, 2018; Revised August 31, 2018 and Accepted September 1, 2018.
*Corresponding author (h.razi@shirazu.ac.ir)

and comparing different unloading models. Livieri and Lazzarin [6] analytically investigated the residual stress distributions for autofrettaged cylindrical vessels considering the Bauschinger effect. Jahed and Ghanbari [7] measured the actual tensile–compressive stress-strain behaviour of steel alloy during the autofrettage process. The significance of employing actual unloading behavior is demonstrated by comparing the results with ideal models such as isotropic hardening and bilinear models. There is at least a 30% overestimation of the compressive residual stress at the bore if ideal models are used.

Zhang et al. [8] using Voroni Cell Finite Element Method by employing Abaqus software studied the effective elastic properties of FG materials. The high-order theory for FG materials was presented by Pindar and Abudi [9]. In 2015, Bayat and Tosy presented the elasto plastic model for the analytical solution of functionally graded hollow cylinders under torsion. In this method, the TTO (Tamura–Tomota–Ozawa) model was used for elastoplastic modeling of functionally graded materials [10]. Majzoobi et al. presented a finite element simulation and an experimental study of autofrettage for strain hardened thick-walled cylinders [11]. In 2015, Kumar and Molik modeled the autofrettage of cylindrical pressure vessels with elliptical cross sections using Ansys FE software [12].

Previous investigations were mainly focused on inducing beneficial residual stresses at the near bore area, neglecting the outer part. However, further investigation of the results indicates that harmful tensile residual stress at the outside layer of the cylinder reduces its carrying load capacity. Moreover, researches mostly focus on static loading while in reality load is applied dynamically and the material behaviour may be drastically different during the transient period due to the elasto-plastic wave propagation and also acoustic impedance. A transient analysis of autofrettage process is consequently necessary to investigate the crucial differences as compared with static results. Such an investigation in thick-walled functionally graded cylinders and an evaluation of the outcome, in particular, the state of residual stresses at the inner as well as the outer part of the cylinder are the subjects of the present paper.

1.1. Explicit Lagrangian method in dynamic autofrettage modeling

An explicit Lagrangian finite difference method is used in the analysis. The governing differential equations are discretized using finite difference method. Toward this end, the equations are integrated, given the geometry and boundary conditions, then by using divergence theorem surface integrals are converted to boundary integrals, and finally the discrete governing equations are presented in explicit Lagrangian formalism. By extracting the explicit transient solution of discrete equations on the meshed region, results for stress and strain distribution are obtained. Finally, the C/C++ numerical programming is prepared using the explicit Lagrangian formalism.

1.2. Equations of motion

In the absence of body force and given the axial symmetry about *z*- axis, the equations of motion are written in cylindrical coordinates as [13]:

$$\begin{cases} \frac{\partial \sigma_{rr}}{\partial r} + \frac{\partial \sigma_{zr}}{\partial z} + \frac{\sigma_{rr} - \sigma_{\theta\theta}}{r} = \rho \frac{\partial^2 U_r}{\partial t^2} \\ \frac{\partial \sigma_{r\theta}}{\partial r} + \frac{\partial \sigma_{z\theta}}{\partial z} + \frac{2\sigma_{r\theta}}{r} = \rho \frac{\partial^2 V_\theta}{\partial t^2} \\ \frac{\partial \sigma_{rz}}{\partial r} + \frac{\partial \sigma_{zz}}{\partial z} + \frac{\sigma_{rz}}{r} = \rho \frac{\partial^2 W_z}{\partial t^2} \end{cases} \quad (1)$$

where U_r, V_θ and W_z are *r*-θ-*z* components of displacement vector, σ stress tensor, *t* time and ρ is density. Using the following relations for the components of velocity and acceleration in radial and tangential directions,

$$\begin{cases} \frac{\partial U_r}{\partial t} = \dot{r} \\ \frac{\partial V_\theta}{\partial t} = r\dot{\theta} \\ \frac{\partial W_z}{\partial t} = \dot{z} \end{cases} \text{و} \begin{cases} \frac{\partial^2 U_r}{\partial t^2} = \ddot{r} - r\dot{\theta}^2 \\ \frac{\partial^2 V_\theta}{\partial t^2} = r\ddot{\theta} + 2\dot{r}\dot{\theta} \\ \frac{\partial^2 W_z}{\partial t^2} = \ddot{z} \end{cases} \quad (2)$$

Equation (1) is simplified to

$$\begin{cases} \frac{d\dot{r}}{dt} = \frac{1}{\rho}\left(\frac{\partial \sigma_{rr}}{\partial r} + \frac{\partial \sigma_{zr}}{\partial z} + \frac{\sigma_{rr} - \sigma_{\theta\theta}}{r}\right) + r\dot{\theta}^2 \\ \frac{1}{r}\frac{d}{dt}\left(r^2\dot{\theta}\right) = \frac{1}{\rho}\left(\frac{\partial \sigma_{r\theta}}{\partial r} + \frac{\partial \sigma_{z\theta}}{\partial z} + \frac{2\sigma_{r\theta}}{r}\right) \\ \frac{d\dot{z}}{dt} = \frac{1}{\rho}\left(\frac{\partial \sigma_{rz}}{\partial r} + \frac{\partial \sigma_{zz}}{\partial z} + \frac{\sigma_{rz}}{r}\right) \end{cases} \quad (3)$$

In Eqs. (3), the variable ρ represents the density of the region in the local coordinates. For functionally graded materials, the mechanical properties of the material change along the *r* direction.

1.3. Conservation of mass

Conservation of mass is written in the form $V_r = \frac{V}{V_0} = \frac{M/\rho}{M/\rho_0} = \frac{\rho_0}{\rho}$ where ρ is the actual density, ρ_0 reference material density, V_r relative volume, M mass, V volume and V_0 initial volume.

1.4. Strain rate components

The components of the strain rate in the cylindrical coordinate *r*-θ-*z* (Lagrangian) are recorded in Eq. (4).

$$\begin{cases} \dot{\varepsilon}_{rr} = \frac{\partial \dot{U}_r}{\partial r} = \frac{\partial \dot{r}}{\partial r} \\ \dot{\varepsilon}_{\theta\theta} = \frac{\dot{U}_r}{r} + \frac{1}{r}\frac{\partial \dot{V}_\theta}{\partial \theta} = \frac{\dot{r}}{r} \\ \dot{\varepsilon}_{zz} = \frac{\partial \dot{W}_z}{\partial r} = \frac{\partial \dot{z}}{\partial z} \\ \dot{\gamma}_{r\theta} = \frac{1}{r}\frac{\partial \dot{U}_r}{\partial \theta} + \frac{\partial \dot{V}_\theta}{\partial r} - \frac{\dot{V}_\theta}{r} = r\frac{\partial \dot{\theta}}{\partial r} \\ \dot{\gamma}_{\theta z} = \frac{\partial \dot{V}_\theta}{\partial z} + \frac{1}{r}\frac{\partial \dot{W}_z}{\partial \theta} = \frac{\partial (r\dot{\theta})}{\partial z} \\ \dot{\gamma}_{zr} = \frac{\partial \dot{U}_r}{\partial z} + \frac{\partial \dot{W}_z}{\partial r} = \frac{\partial \dot{r}}{\partial z} + \frac{\partial \dot{z}}{\partial r} \end{cases} \quad (4)$$

1.5. Deviatoric stress rate components

The deviatoric stress rate components are recorded in Eq. (5).

$$\begin{cases} \dot{s}_{rr} = 2\mu\left(\dot{\varepsilon}_{rr} - \frac{1}{3}\frac{\dot{V}}{V}\right) \\ \dot{s}_{\theta\theta} = 2\mu\left(\dot{\varepsilon}_{\theta\theta} - \frac{1}{3}\frac{\dot{V}}{V}\right) \\ \dot{s}_{zz} = 2\mu\left(\dot{\varepsilon}_{zz} - \frac{1}{3}\frac{\dot{V}}{V}\right) \\ \dot{\sigma}_{r\theta} = \mu\dot{\gamma}_{r\theta} \\ \dot{\sigma}_{\theta z} = \mu\dot{\gamma}_{\theta z} \\ \dot{\sigma}_{zr} = \mu\dot{\gamma}_{zr} \end{cases} \quad (5)$$

1.6. Rate of hydrostatic pressure

The time rate of hydrostatic pressure is

$$\dot{p} = -k\left(\frac{\dot{V}}{V}\right) \quad (6)$$

where *k* is the bulk modulus of elasticity.

1.7. Total stress components

The normal components of the total stress are

$$\begin{cases} \sigma_{rr} = -(p+q) + s_{rr} \\ \sigma_{\theta\theta} = -(p+q) + s_{\theta\theta} \\ \sigma_{zz} = -(p+q) + s_{zz} \end{cases} \tag{7}$$

where p and q are hydrostatic pressure and artificial viscosity [14].

1.8. von-Mises yield condition

If Y is the plastic flow stress and J_2 the second invariant of deviatoric stress tensor, then

$$\sqrt{2J_2} - \sqrt{\frac{2}{3}}Y \leq 0 \tag{8}$$

1.9. Elasto-plastic model for functionally graded materials

The mechanical properties of functionally graded materials for elasto-plastic deformation are assumed to change according to

$$P = P_m + (P_c - P_m)V_f \,, \tag{9}$$

where $V_f = f_0((r-r_i)/(r_o-r_i))^n$ is the volume fraction for cylindrical geometry along the cylinder thickness in which r_o and r_i are the outer and inner radii of the cylinder respectively, n is the reinforcement distribution exponent and f_0 a distribution coefficient.

The plastic flow model can also be expressed as [15]

$$\sigma_e = \sigma_y(r) + h_p(r)(\varepsilon_e^p)^{n_y}, \; h_p = \frac{EH}{E-H}, \tag{10}$$

where σ_e is the equivalent stress, σ_y yield stress, h_p plasticity modulus or the gradient of stress-plastic strain curve, ε_e^p equivalent plastic strain, n_y hardening exponent, E module of elasticity, and H the tangent modulus. The stress strain curves for the constituents are shown in Fig. 1.

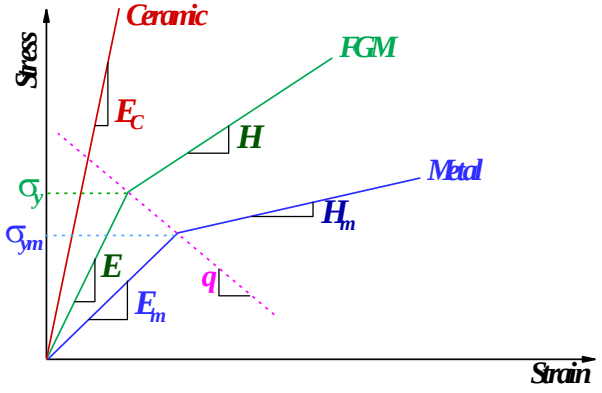

Fig. 1. Stress-strain curve for FG materials [15].

The mechanical parameters for FG materials in the elasto-plastic state are expressed in Eqs. (11) - (13). Subscripts c and m denote ceramic and metal, q_r is the stress to strain ratio defined by $q_r = (\sigma_c - \sigma_m)/|\varepsilon_c - \varepsilon_m|$, where E is the modulus of elasticity, σ_y the initial yield stress and H the tangent modulus [15].

$$E = \left[(1-V_f)E_m\frac{q_r+E_c}{q_r+E_m} + V_f E_c\right]\left[(1-V_f)\frac{q_r+E_c}{q_r+E_m} + V_f\right]^{-1} \tag{11}$$

$$\sigma_y = \sigma_{ym}\left[(1-V_f)\frac{q_r+E_m}{q_r+E_c}\frac{E_c}{E_m}V_f\right] \tag{12}$$

$$H = \left[(1-V_f)H_m \frac{q_r+E_c}{q_r+H_m} + V_f E_c\right]\left[(1-V_f)\frac{q_r+E_c}{q_r+H_m} + V_f\right]^{-1} \quad (13)$$

2. Computational Sequences in Lagrangian Method

2.1. Finite difference and contour integral

A Lagrangian calculation scheme embeds a computational mesh in the material domain and solves the position of the mesh at discrete points in time. The method that is currently used for solving transient hydrodynamic problems is explicit. The solution is improved by altering the time from t^n to t^{n+1} without any iterations, and the time step is denoted by $\Delta t^{n+1/2}$. This is based on the second order accurate central difference approximation, which is readily derived from Taylor series expansion. A superscript *n* indicates that the function is evaluated at t^n. The time step size is a function of both the element geometry and sound speed within the material [16].

The two-dimensional mesh used to extract the governing equations is shown in Fig. 2. Two intersecting sets of lines called j and k lines define a set of quadrilaterals. The quadrilateral regions bounded by the four nodes are called zones (for example 1). They are labelled by the average logical coordinates of the nodes, (j+1/2, k+1/2). The displacements, velocities and accelerations are evaluated at the nodes, while the remaining variables are evaluated at the centroids of the zones.

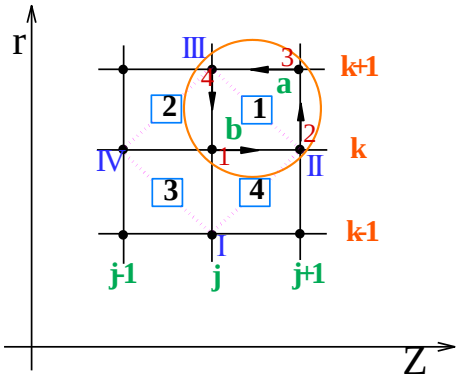

Fig. 2. Two-dimensional mesh used to extract the governing equations.

Based on what has been said, for dynamic equations the finite difference relations will be in accordance with Eq. (14). The integration path from nodes I to IV is shown on the dotted line in Fig. 2. It should be noted that in this case, the values of F (arbitrary function) are in the center of the region; this mode is used to calculate the velocity in the nodes based on the stress in the center of the zone. *A* is the area enclosed by the integration paths I, II, III, IV and is taken as the average of the area contributions of the four zones surrounding point 1. **n** is the unit vector perpendicular to the boundary domain, $\mathbf{e_r}$ and $\mathbf{e_k}$ are unit vectors in r and z directions.

$$\begin{cases} \left.\frac{\partial F}{\partial r}\right|_1 = \lim_{A\to 0}\int_{(C)} \frac{F(\mathbf{n}.\mathbf{e_r})dl}{A} = -\frac{\int_{(C)} F(\mathbf{n}.\mathbf{e_r})dl}{A} \\ \left.\frac{\partial F}{\partial z}\right|_1 = \lim_{A\to 0}\int_{(C)} \frac{F(\mathbf{n}.\mathbf{e_k})dl}{A} = \frac{\int_{(C)} F(\mathbf{n}.\mathbf{e_k})dl}{A} \end{cases} \quad (14)$$

In Eq. (14), i and j are unit vectors along the axes *z* and *r*, (C) is the integral path from I to IV according to the dotted line shown in Fig. 2. For node 1, then the difference equations are

$$\int_{(C)} F(\mathbf{n}.\mathbf{e_r})dl = +[F_{\boxed{1}}(r_{II}-r_{III}) + F_{\boxed{2}}(r_{III}-r_{IV}) + F_{\boxed{3}}(r_{IV}-r_I) + F_{\boxed{4}}(r_I-r_{II})] \quad (15)$$

$$\int_{(C)} F(\mathbf{n}.\mathbf{e_k})dl = +[F_{\boxed{1}}(z_{II}-z_{III}) + F_{\boxed{2}}(z_{III}-z_{IV}) + F_{\boxed{3}}(z_{IV}-z_I) + F_{\boxed{4}}(z_I-z_{II})] \quad (16)$$

The path of integration in this case for zone 1 is shown from nodes 1 through 4 on the directional path. It should be noted that in this case the F values are in the nodes and this mode is used to calculate the strain rate in the center of the zone, based on the speed in nodes 1 to 4, which encloses the zone. The integral results for F are given by $\mathrm{F_{pq}} = \frac{1}{2}(\mathrm{F_p} + \mathrm{F_q})$ in accordance with Eq. (17) and Eq. (18).

$$\left.\frac{\partial \mathrm{F}}{\partial r}\right|_{\boxed{1}} = \frac{\int_{(C)} \mathrm{F}(\mathbf{n}.\mathbf{e_r})dl}{A} = -\frac{1}{A}[\mathrm{F}_{31}(z_3 - z_1) + \mathrm{F}_{34}(z_3 - z_4) + \mathrm{F}_{41}(z_4 - z_1) + \mathrm{F}_{12}(z_1 - z_2)] = -\frac{1}{2A}[(\mathrm{F}_2 - \mathrm{F}_4)(z_3 - z_1) - (z_2 - z_4)(\mathrm{F}_3 - \mathrm{F}_1)] \quad (17)$$

$$\left.\frac{\partial \mathrm{F}}{\partial z}\right|_{\boxed{1}} = \frac{\int_{(C)} \mathrm{F}(\mathbf{n}.\mathbf{e_k})dl}{A} = +\frac{1}{2A}[(\mathrm{F}_2 - \mathrm{F}_4)(r_3 - r_1) - (r_2 - r_4)(\mathrm{F}_3 - \mathrm{F}_1)] \quad (18)$$

2.2. Volume zone

The problem is formulated in *r* and *z* coordinates with the cylindrical symmetry about *z*-axis, including rotation. The volume of each zone is

$$\begin{cases} V_{\boxed{1}} = \bar{Y}_a A_a + \bar{Y}_b A_b\,,\ A_{\boxed{1}} = A_a + A_b \\ \bar{Y}_a = \frac{1}{3}(r_2 + r_3 + r_4) \\ \bar{Y}_b = \frac{1}{3}(r_1 + r_2 + r_4) \\ A_a = \frac{1}{2}[z_2(r_3 - r_4) + z_3(r_4 - r_2) + z_1(r_2 - r_3)] \\ A_b = \frac{1}{2}[z_2(r_4 - r_1) + z_4(r_1 - r_2) + z_1(r_2 - r_4)] \end{cases} \quad (19)$$

z_i and r_i are the general coordinates of node i, V_i 's are the volume of the rotated region around *z*-axis, *A* is the zone area, and a and b represent the triangle formed within the region, as shown in Fig. 2.

2.3. Conservation of mass

To calculate the mass of zone 1, we have

$$M_{\boxed{1}} = \left(\frac{\rho_0}{V_r^0} V^0\right)_{\boxed{1}} \quad (20)$$

ρ_0 is the initial density, V_r^0 is the initial relative volume and V^0 is the real initial volume obtained from the calculation of the zone volume at time $t = 0$.

2.4. Equations of motion

The discrete form of equations of motion in *r* direction is presented in Eq. (21), and likewise for other directions.

$$\dot{r}_{j,k}^{n+\frac{1}{2}} = \dot{r}_{j,k}^{n-\frac{1}{2}} + \frac{\Delta t^n}{2\varphi_{j,k}^n}\Big[(\sigma_{rr})_{\boxed{1}}^n(z_{II}^n - z_{III}^n) + (\sigma_{rr})_{\boxed{2}}^n(z_{III}^n - z_{IV}^n) + (\sigma_{rr})_{\boxed{3}}^n(z_{IV}^n - z_I^n) + (\sigma_{rr})_{\boxed{4}}^n(z_I^n - z_{II}^n) - (\sigma_{zr})_{\boxed{1}}^n(r_{II}^n - r_{III}^n) - (\sigma_{zr})_{\boxed{2}}^n(r_{III}^n - r_{IV}^n) - (\sigma_{zr})_{\boxed{3}}^n(r_{IV}^n - r_I^n) - (\sigma_{zr})_{\boxed{4}}^n(r_I^n - r_{II}^n)\Big] + \Delta t^n[(\beta)_{j,k}^n + \left(\omega_{j,k}^n\right)^2 r_{j,k}^n] \quad (21)$$

where

$$\varphi_{j,k}^n = \frac{1}{4}\left[\left(\frac{\rho_0 A^n}{V_r^n}\right)_{\boxed{1}} + \left(\frac{\rho_0 A^n}{V_r^n}\right)_{\boxed{2}} + \left(\frac{\rho_0 A^n}{V_r^n}\right)_{\boxed{3}} + \left(\frac{\rho_0 A^n}{V_r^n}\right)_{\boxed{4}}\right] \quad (22)$$

$$\beta_{j,k}^n = \frac{1}{4}\left\{\left[(\sigma_{rr}^n - \sigma_{\theta\theta}^n)\left(\frac{A^n}{M}\right)\right]_{\boxed{1}} + \left[(\sigma_{rr}^n - \sigma_{\theta\theta}^n)\left(\frac{A^n}{M}\right)\right]_{\boxed{2}} + \left[(\sigma_{rr}^n - \sigma_{\theta\theta}^n)\left(\frac{A^n}{M}\right)\right]_{\boxed{3}} + \left[(\sigma_{rr}^n - \sigma_{\theta\theta}^n)\left(\frac{A^n}{M}\right)\right]_{\boxed{4}}\right\} \quad (23)$$

$$r_{j,k}^{n+1} = r_{j,k}^{n} + \dot{r}_{j,k}^{n+\frac{1}{2}} \Delta t^{n+\frac{1}{2}} \tag{24}$$

2.5. Strain rate components

The discrete form for the components of the strain rate tensor is presented in Eqs. (25) and (26). The same procedure is followed for other components.

$$(\dot{\varepsilon}_{rr})_{\boxed{1}}^{n+\frac{1}{2}} = (\frac{\partial \dot{r}}{\partial r})_{\boxed{1}}^{n+\frac{1}{2}} = \frac{-1}{2A_{\boxed{1}}^{n+\frac{1}{2}}} [(\dot{r}_2 - \dot{r}_4)(z_3 - z_1) - (z_2 - z_4)(\dot{r}_3 - \dot{r}_1)]_{\boxed{1}}^{n+\frac{1}{2}} \tag{25}$$

$$(\Delta\varepsilon_{rr})_{\boxed{1}}^{n+\frac{1}{2}} = (\dot{\varepsilon}_{rr})_{\boxed{1}}^{n+\frac{1}{2}} \Delta t^{n+\frac{1}{2}} \tag{26}$$

2.6. Stress components

The stress deviator is

$$(s_{rr})_{\boxed{1}}^{n+1} = (s_{rr})_{\boxed{1}}^{n} + 2\mu_{\boxed{1}} \left[\Delta\varepsilon_{rr}^{n+\frac{1}{2}} - \frac{1}{2}\left(\frac{\Delta V_r}{V_r}\right)^{n+\frac{1}{2}}\right]_{\boxed{1}} + (\delta_{rr})_{\boxed{1}}^{n} \tag{27}$$

If a mass element is rotated in *r*-*z* plane by angle ω_r during time interval, the stresses must be recalculated so that they conform with *r* and *z* coordinate system in their new positions. The following transformation equations are used [17].

$$\sin(\omega_r) = \frac{\Delta t^{n+\frac{1}{2}}}{2A_{\boxed{1}}^{n+\frac{1}{2}}} \{[(\dot{r}_2 - \dot{r}_4)(r_3 - r_1) - (r_2 - r_4)(\dot{r}_3 - \dot{r}_1)] - [(\dot{z}_2 - \dot{z}_4)(z_3 - z_1) - (z_2 - z)(\dot{z}_3 - \dot{z}_1)]\}_{\boxed{1}}^{n+\frac{1}{2}} \tag{28}$$

$$\delta_{rr}^{n} = -\left(\frac{s_{zz}^{n} - s_{rr}^{n}}{2}\right)(\cos(2\omega_r) - 1) + \sigma_{zr}^{n} \sin(2\omega_r) \tag{29}$$

and the total stress is

$$(\sigma_{rr}^{n+1})_{\boxed{1}} = (s_{rr})_{\boxed{1}}^{n+1} + \left(p^{n+1} + q^{n+\frac{1}{2}}\right)_{\boxed{1}}, \tag{30}$$

where *p* and *q* are hydrostatic pressure and artificial viscosity, respectively. Other components are given in the same manner.

2.7. Von-Mises yield condition and equivalent plastic strain

The von Mises yield criteria to check the flow and correct stresses are

$$2J^{n+1} = (s_{zz}^{n+1})^2 + (s_{rr}^{n+1})^2 + \left(s_{\theta\theta}^{n+1}\right)^2 + 2[(\sigma_{zr}^{n+1})^2 + \left(\sigma_{r\theta}^{n+1}\right)^2 + \left(\sigma_{\theta z}^{n+1}\right)^2] \tag{31}$$

$$m^{n+1} = \sqrt{\frac{2}{3}} \frac{(Y^0)^n}{\sqrt{2J^{n+1}}} \ , \tag{32}$$

where Y^0 is the flow stress, calculated from a constitutive equation that describes the material behavior. If $m^{n+1} < 1$, multiply each deviatoric stress by m^{n+1}. If $m^{n+1} \geq 1$, use the stresses as they are for the next step. The change in the plastic strain is defined by [18]

$$(\Delta\varepsilon^p)^{n+1} = \left(\frac{1}{m^{n+1}} - 1\right)\left(\frac{Y^0}{3\mu}\right)^n, \tag{33}$$

where $\Delta\varepsilon^p \geq 0$ and μ is the shear modulus.

2.8. Artificial viscosity [14, 19]

The artificial viscosity, q used here, is composed of a quadratic term ${c_0}^2\rho L^2\left(\frac{dS}{dt}\right)^2$ and a linear term $c_L\rho La\left|\frac{dS}{dt}\right|$ in the zone that the rate of strain is negative and $\frac{dS}{dt}$ is the rate of strain in the direction of acceleration [14].

$$\frac{dS}{dt}=\frac{\partial\dot{z}}{\partial z}\cos^2(\alpha)+\frac{\partial\dot{r}}{\partial r}\sin^2(\alpha)+(\frac{\partial\dot{z}}{\partial r}+\frac{\partial\dot{r}}{\partial z})\cos(\alpha)\sin(\alpha) \tag{34}$$

$$\cos(\alpha)=\frac{A_z}{\sqrt{{A_z}^2+{A_r}^2}}\ ,\ \ \sin(\alpha)=\frac{A_r}{\sqrt{{A_z}^2+{A_r}^2}} \tag{35}$$

$$\mathrm{A_z}=\dot{z}^{n+\frac{1}{2}}-\dot{z}^{n-\frac{1}{2}}\ ,\ \ \mathrm{A}_r=\dot{r}^{n+\frac{1}{2}}-\dot{r}^{n-\frac{1}{2}} \tag{36}$$

$$\begin{cases} q={c_0}^2\rho L^2\left(\frac{dS}{dt}\right)^2+c_L\rho La\left|\frac{dS}{dt}\right| & \frac{dS}{dt}<0 \\ q=0 & \frac{dS}{dt}\geq 0 \end{cases} \tag{37}$$

For problems in solid mechanics, nonphysical numerical oscillations can occur in the grid under certain boundary conditions. A tensor viscosity based on the rate of the strain of volume elements formed by the zone comers is used to damp this type of oscillation. The existence and nature of the hourglass modes can be deduced from very primitive considerations. We have used the "triangle Q" of Wilkins [14, 19] or Navier-Stockes artificial viscosity for the stabilizing grid.

2.9. Time step calculation

The time step size for the central difference integration method is determined by stability considerations. In hydrodynamic problems, the typical stable step sizes are so small that accuracy is not a consideration. For two dimensions, the following stability condition is used [14]

$$\Delta t^{n+\frac{3}{2}}=0.67\frac{L^{n+1}}{\sqrt{a^2+b^2}}\Big|_{Minimum\ of\ All\ Zones} \tag{38}$$

a is the sound speed and $b=8[c_0^2+c_L]L^{n+1}\left|\frac{dS}{dt}\right|$, where c_0^2 and c_L are the quadratic and the linear q constants, respectively.

2.10. Boundary conditions and loadings

Pseudo zones with zero mass are assumed to surround the grid that defines the physical domain. Thus the points associated with the surface of the physical domain may be located without changing the logic. Normally, a free surface boundary condition is provided. Here the pseudo zone pressures are always considered equal to zero. Phantom zones are created by a mirror reflection cross the boundary and setting the normal component of the accelerations at the surface point to zero. Transient pressure boundary conditions may be applied by entering the desired space-time values into the pseudo zones.

3. Numerical results

In order to verify the accuracy of the numerical code, the test problems, for which the theoretical, numerical and experimental results are known, are examined. Following that, the results of single and double autofrettage in the FG cylinder are presented.

3.1. Residual stress distribution and verification of the presented method

A bilinear hardening model approximating the real material behavior (NiCrMoV125) [16] has been used. The material constants and cylinder dimensions are as follows:

$$(r_i=14.60\ \mathrm{cm}, r_o=30.50\ \mathrm{cm})$$

$$\rho=7800.00\ \mathrm{kg/m^3}\ , E=268.0\ \mathrm{GPa}\ , \nu=0.29,$$
$$Y=700.0\ \mathrm{MPa}, H=75\ \mathrm{GPa}, n_y=1.0$$

The non-dimensional residual hoop stress distribution through the thickness of the cylinder has been evaluated for the autofrettage pressure of 736 MPa (Fig. 3), and then it is compared with that in Refs. [7, 20], as shown in Fig. 4.

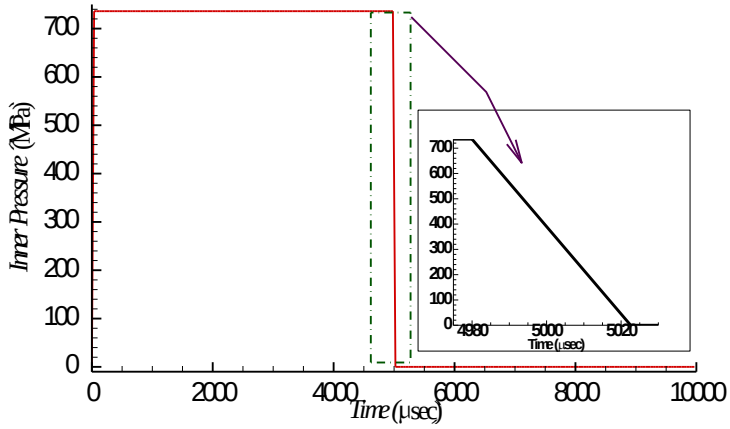

Fig. 3. Transient load curve for autofrettage.

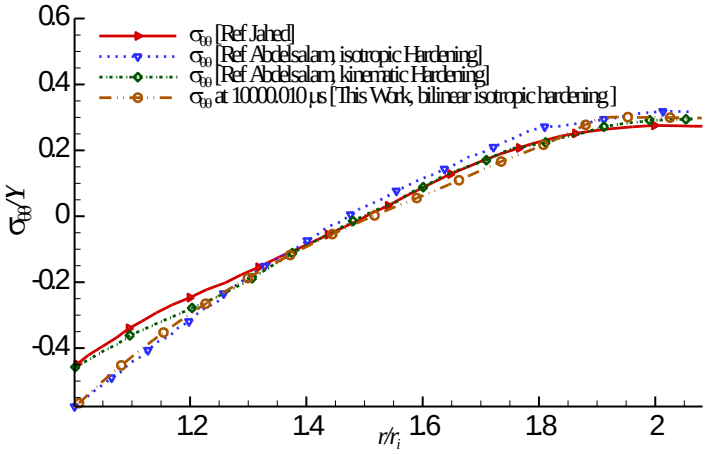

Fig. 4. Residual stress resulting from the experimental, numerical and the current method [7, 20].

As it can be seen from Fig. 4, the predicted residual hoop stress distribution through the thickness based on the bilinear hardening model shows good agreement with other results.

3.2. Difference between dynamic and static modeling in autofrettage

In order to analyze the dynamic modeling and compare the results with the static solution in the process of autofrettage, we consider the geometric and mechanical properties of the cylinder as follows (used in Waterjet Cut Tools Nozzle).

$$(r_i = 0.150 \text{ cm}, r_o = 0.475 \text{ cm})$$

$$\rho = 7800.00 \text{ kg/m}^3 \text{ , } E = 200.0 \text{ GPa , } \nu = 0.3,$$

$$Y = 280.0 \text{ MPa}, H = 0.22698 \text{ GPa}, n_y = 0.43$$

The transient internal pressure is applied from 100 to 140 MPa at the inner radius of the cylinder and the stress results are compared for static and dynamic modeling. After applying the internal pressure, a plastic strain zone is created as shown in Fig. 5.

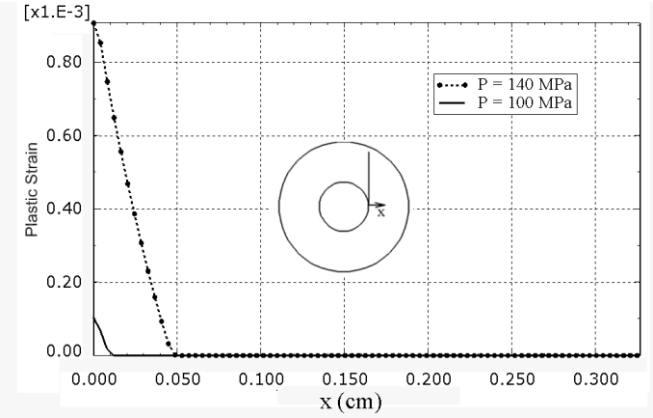

Fig. 5. The plastic range for transient loading mode.

In Fig. 6 the distribution of hoop stress is shown along the radius for transient modeling and internal pressure of 140 MPa

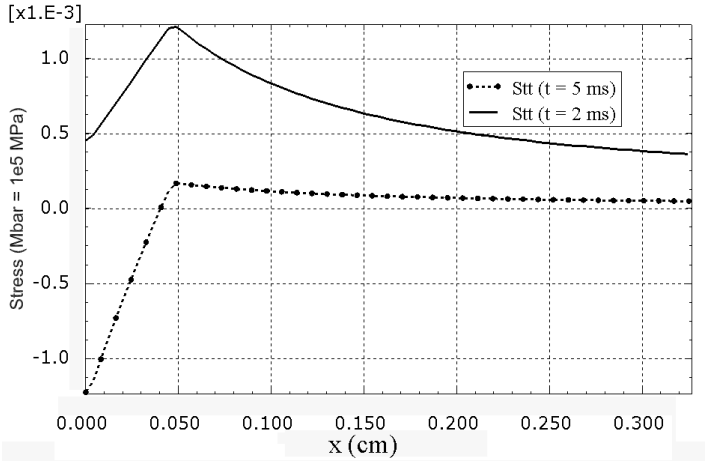

Fig. 6. Hoop stress distribution for transient load P = 140 MPa.

The results for static analysis of this problem were carried out using the Abaqus finite element software [21]. The distribution of the stress for the static analysis is shown in Fig. 7.

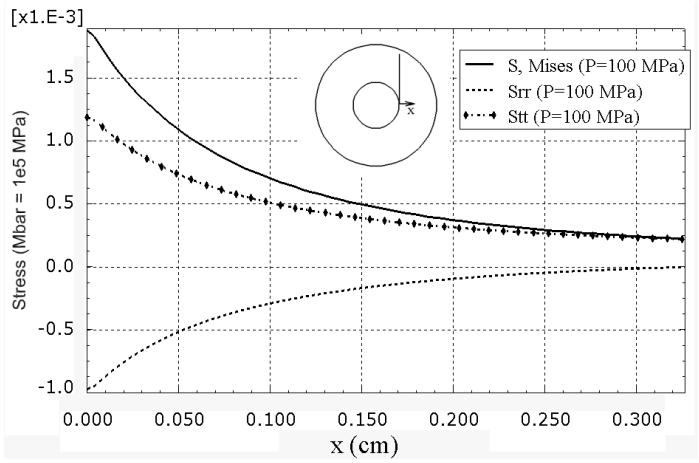

Fig. 7. Distribution of the stress in the static analysis for p=140MPa (Abaqus FE software).

As can be seen, the stress distribution is completely different and the deformation in this pressure range is within the elastic range but a result of the dynamic analysis indicates the formation of the plastic zone near the bore area.

3.3. Numerical analysis of single and double autofrettage in FG cylinder

To study the effect of dynamic autofrettage in FG cylinder, a functionally graded material with the combination of NiCrAlY metal and PSZ ceramic is chosen. The mechanical properties are:

$$\rho_m = 7800.00\ \text{kg/m}^3\ , E_m = 56.0\ \text{GPa}\ , \upsilon_m = 0.25,$$
$$Y_m = 106.0\ \text{MPa}, H_m = 12\ \text{GPa}, n_{ym} = 1.0$$
$$\rho_c = 2370.00\ \text{kg/m}^3\ , E_c = 80, \upsilon_c = 0.25,$$

Case 1- Single autofrettage: $r_i = 10$ cm, $r_o = 20$ cm

In this case, for FG cylinder, a combination of the inner metal layer and the outer ceramic layer is used. The internal pressure changes from 60 MPa to 90 MPa. The 40 MPa working pressure is applied and this pressure is normally in the elastic range. Figure 8 shows the time dependent internal pressure loading.

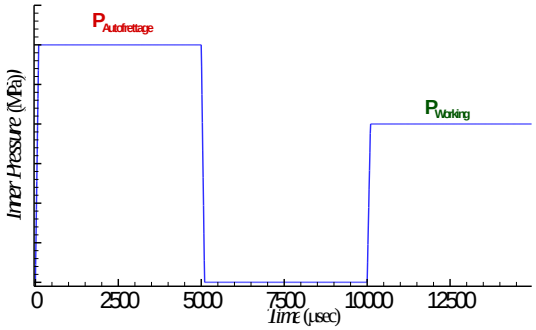

Fig. 8. Autofrettage and working pressure.

In Fig. 9 and Fig. 10, the distribution of the plastic strain along the thickness of the cylinder is shown after the completion of the autofrettage process.

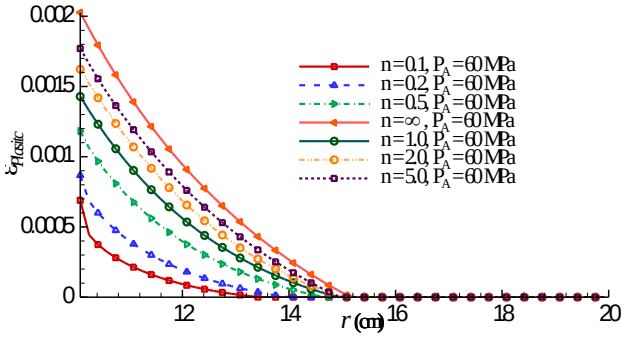

Fig. 9. Plastic strain distribution for FG materials subject to the same pressure.

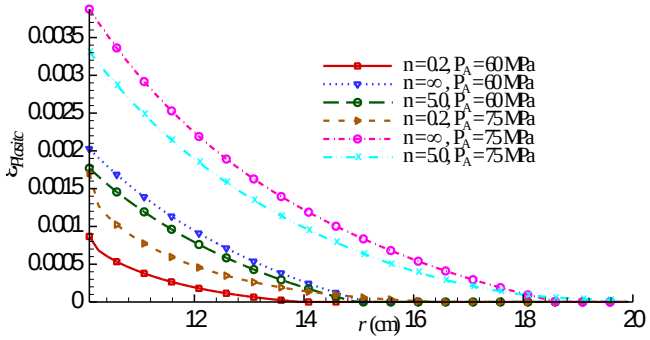

Fig. 10. Plastic strain distribution for FG materials under different pressures.

Figures 9 and 10 indicate that increasing the coefficient *n* will increase the magnitude and range of the plastic strain along the thickness. The largest amount of the plastic strain occurs for metal ($n=\infty$).

The particle velocity for the inner radius and for various compositions of the FG material are shown in Figs. 11 and 12. As *n* increases, the amplitude and frequency of the wave decrease while its damping rate increases.

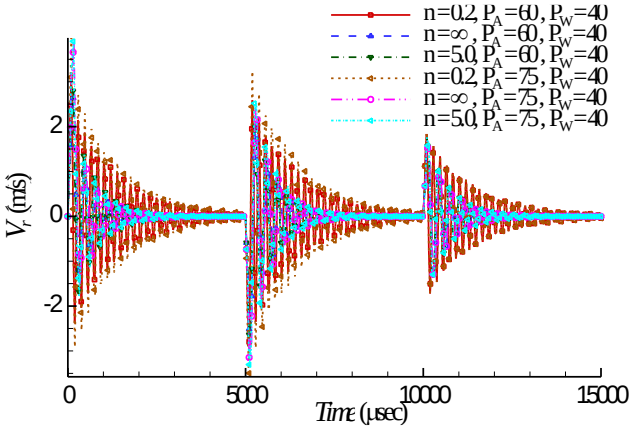

Fig. 11. Particle velocity at the inner radius.

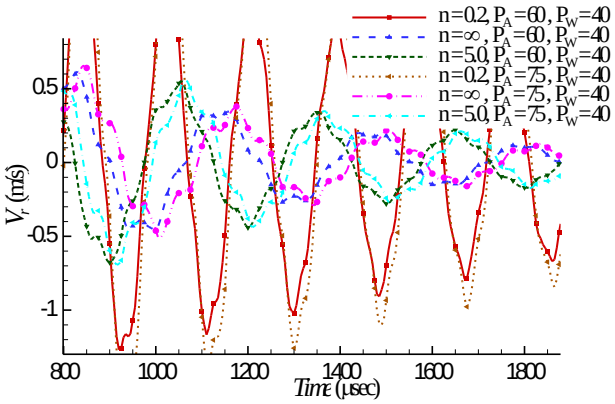

Fig. 12. Magnification of Fig. 11.

In Figs. 13 and 14, the distribution of hoop stress for different autofrettage pressures is shown.

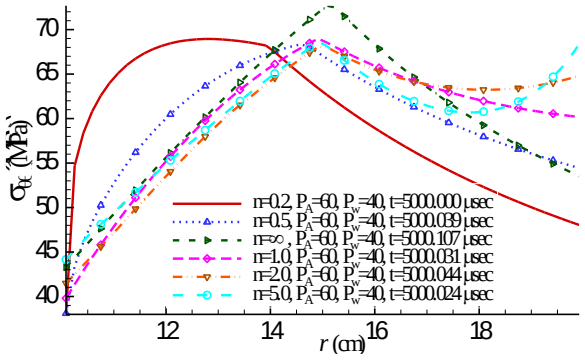

Fig. 13. Distribution of hoop stress at 5 ms for different coefficients.

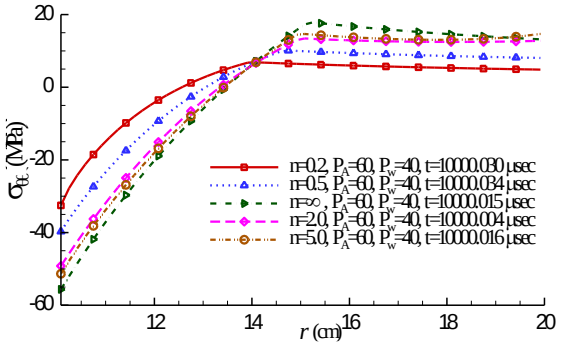

Fig. 14. Distribution of residual hoop stress at 10 ms.

After the completion of the autofrettage process, working pressure is applied and the resultant hoop stress is shown in Fig. 15.

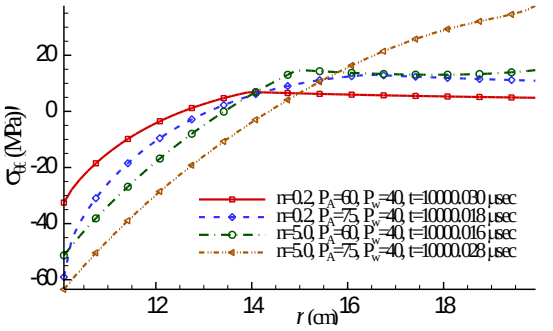

Fig. 15. Distribution of the resultant hoop stress under working pressure after autofrettage.

Case 2- Single autofrettage: $r_i = 1$ cm, $r_o = 2$ cm

In order to investigate the effect of geometry, the internal and external radii are considered one-tenth of the previous case. Residual stresses are compared in Fig. 16.

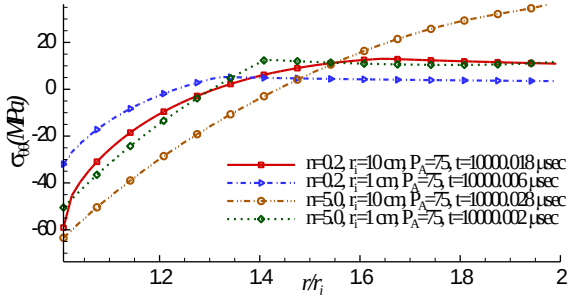

Fig. 16. Effect of geometry on the residual hoop stress distribution.

As Fig. 16 shows, reducing the size of the cylinder results in a completely different distribution of the residual hoop stress. If the coefficient of the distribution f_0 changes for a FG material, the range of the plastic strain will also change, as shown in Fig. 17.

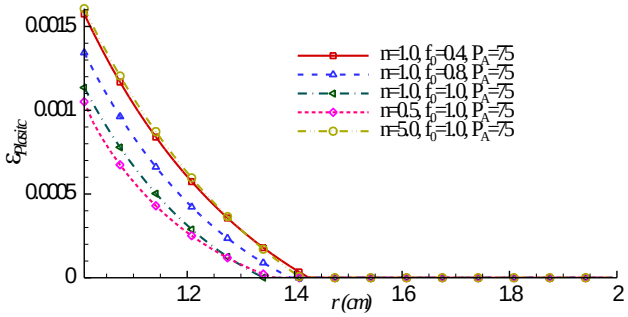

Fig. 17. Range of the plastic strain radius based on the distribution coefficient (r_i = 1 cm).

In Figs. 18 and 19, the residual hoop stress is shown for different conditions along the thickness.

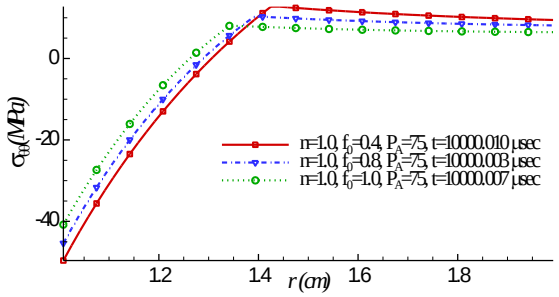

Fig. 18. Distribution of the residual hoop stress for different distribution coefficients.

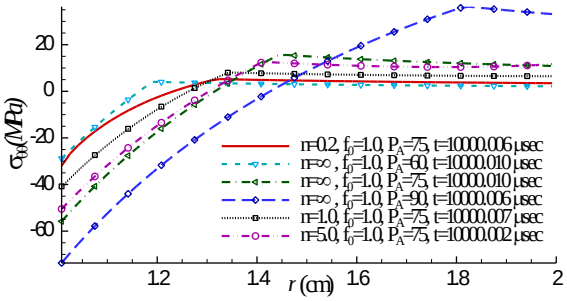

Fig. 19. Distribution of the residual hoop stress for different autofrettage pressures.

Case 3- Double autofrettage: $r_i = 10$ cm, $r_o = 20$ cm

In the double autofrettage, an external surface autofrettage process is performed prior to the conventional inner surface process. In order to investigate the double autofrettage and compare the results with those of the single autofrettage in FG cylinder, we assume the FG material properties and dimension presented in case 1 (NiCrAlY metal and PSZ ceramic). The external pressure and internal pressure changes from 35 MPa to 70 MPa and Fig. 20 shows the time dependent external (p_o) and internal (p_i) pressure loadings.

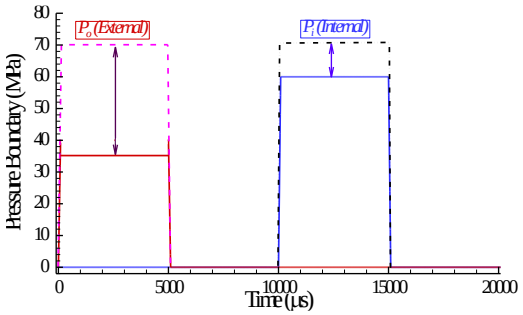

Fig. 20. Double autofrettage pressure loading curve scheme.

The distributions of the plastic strain along the thickness of the cylinder after the completion of the double autofrettage process for various FG parameters are shown in Figs. 20 and 22.

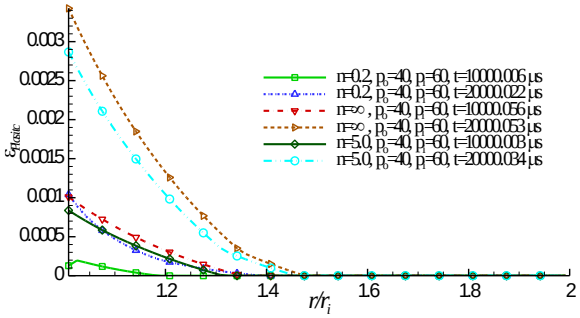

Fig. 21. Plastic strain distribution of the double autofrettage at the same pressure and different *n*.

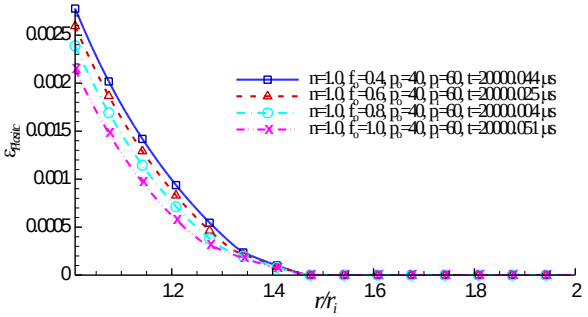

Fig. 22. Plastic strain distribution of the double autofrettage at the same pressure with different f_0 and n=1.0.

In Figs. 23-26, the distribution of the hoop stress for different double autofrettage pressures and FG parameters are shown.

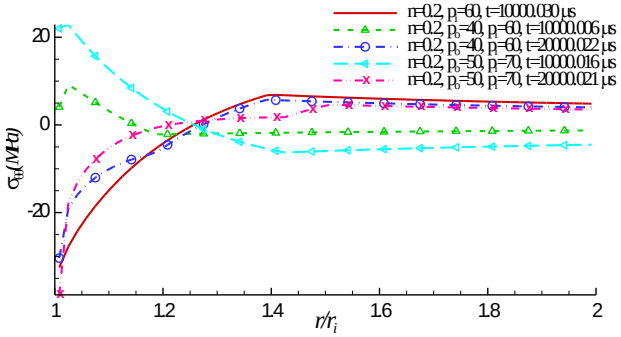

Fig. 23. Distribution of the residual hoop stress in single and double autofrettage at 10 ms and 20 ms for n=0.2.

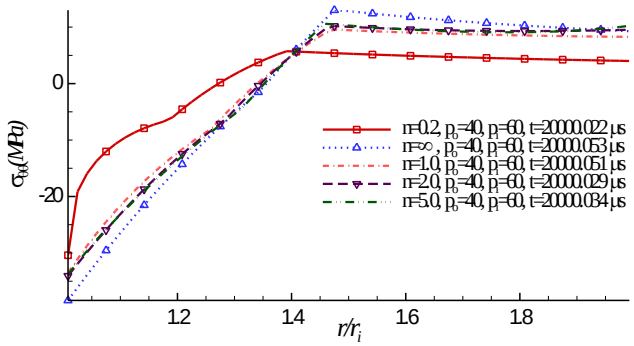

Fig. 24. Distribution of the residual hoop stress in the double autofrettage at 20 ms and the same pressure.

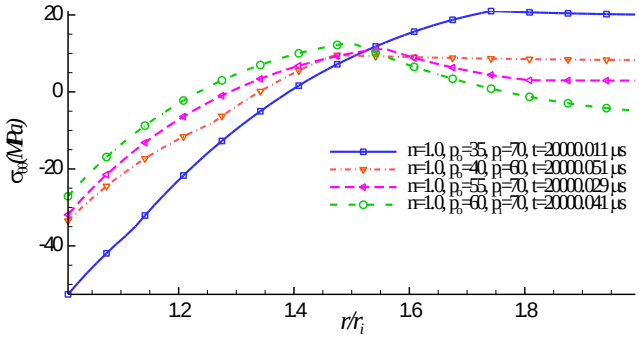

Fig. 25. Distribution of residual hoop stresses in the double autofrettage for (f_0 = 1.0, n=1.0) and different pressures.

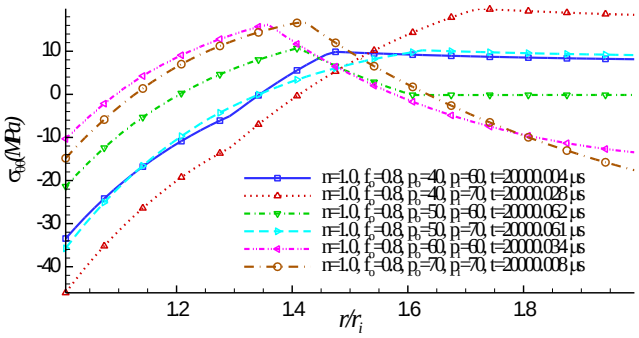

Fig. 26. Residual hoop stresses distribution in the double autofrettage process (f_0 = 0.8, n=1.0) with different pressures.

As Figs. 25 and 26 indicate, a combination of external and internal pressures results in compressive residual hoop stress in the internal radius and tensile residual hoop stress in the external radius. These pressures can be controlled to obtain the desired results.

4. Conclusions

Numerical results presented in the previous section are indicative of the importance of the dynamical analysis in investigating the process of autofrettage. To examine the role of the stress waves generated due to dynamical loading, the actual size of the cylinder becomes a crucial factor. This is in contrast to the static analysis in which the dimensionless forms of the equations can be formed from the onset.

As for the FG material, the reinforcement distribution exponent n plays an important role in the structural response (the plastic zone, magnitude of the stress). Decreasing n results in the reduction of the tensile stresses in the outer area. At the same time, the maximum compressive stress in the inner radius does not change significantly, while the distribution of the hoop stress changes in the thickness.

Previous works often focused on increasing the magnitude of the compressive residual stress at the inner layer or near the bore area of the thick-walled FG cylinders, while ignoring the harmful high tensile residual stress at the outer part, which can reduce the fatigue life. Given the importance of such a consideration, for a specific loading, a combination of FG materials can be chosen that results in a higher compressive residual hoop stress in the inner radius and lower tensile residual hoop stress in the outer radius of the cylinder. In general, all dynamic parameters, including loading time, material properties and actual geometry, will play important roles in the responses. To summarize:

1- Dynamic analysis shows different results as compared with the static analysis when plastic deformation is involved. As the damping coefficient increases, results approach their static counterparts

2- In dynamic analysis of autofrettage, the actual size is crucial in evaluating the residual stresses and plastic strain, although it is anticipated that when the actual size reduces, these effects become less important.

3- In the double autofrettage, by changing external and internal pressures, it is possible to control the variation of tensile and compressive residual hoop stresses better, while in the single autofrettage only the internal stress is controlled and the external stress is determined using the appropriate boundary conditions and it is not individually controllable. As a result, the double autofrettage gives the designer more flexibility to enforce the appropriate residual stress in the cylinder in such a way that the tensile residual hoop stress of the outer part is reduced and the suitable internal compressive residual hoop stress is produced to meet the working condition.

5. References

[1] G. J. Franklin, J. L. M. Morrison, Autofrettage of Cylinders: Prediction of Pressure, External Expansion Curves and Calculation of Residual Stresses, *Proceeding of Institute of Mechanical Engineers*, 174 (1960) 947–74.

[2] P. C. T. Chen, Stress and Deformation Analysis of Autofrettaged High Pressure Vessels, *ASME special publication PVP New York ASME United Engineering Center,* (1986) 61–70.

[3] Stacey, G. A. Webster, Determination of Residual Stress Distributions in Autofrettaged Tubing, *International Journal of Pressure Vessels and Piping* 31 (1988) 205–220.

[4] D. W. A. Rees, Autofrettage of thick-walled pipe bends, *International Journal of Mechanical Sciences* 46 (2004) 1675–1696.

[5] P. Parker, Autofrettage of Open-End Tubes-Pressures, Stresses, Strains, and Code Comparisons, *Journal of Pressure Vessel Technology* 123 (2001) 271–281.

[6] P. Livieri, P. Lazzarin, Autofrettaged Cylindrical Vessels and Bauschinger Effect: an Analytical Frame for Evaluating Residual Stress Distributions, *Transaction ASME Journal of Pressure Vessel Technology* 124 (2002) 38–45.

[7] H. Jahed, G. Ghanbari, Actual Unloading Behavior and Its Significance on Residual Stress in Machined Autofrettaged Tube, *ASME J. Pressure Vessel Technol.* 125 (2003) 321–325.

[8] M. Grujicic, Y. Zhang, Determination of effective elastic properties of Functionally Graded Materials using Voroni Cell Finite Element Method, *Materials Science and Engineering* A 251 (1998) 64-76.

[9] J. Aboudi, M. Pindera, S. M. Arnold, Higher-order theory for Functionally Graded Materials, *Composites: Part B* 30 (1999) 777-832.

[10] Y. Bayat, H. Ekhteraei Toussi, Elastoplastic torsion of hollow FGM circular shaft, *Journal of Computational and Applied Research in Mechanical Engineering* 4 (2015) 165-180.

[11] G. H. Majzoobi, G. H. Farrahi, A. H. Mahmoudi, A finite element simulation and an experimental study of Autofrettage for strain hardened thick-walled cylinders, *Materials Science and Engineering* A359 (2003) 326-331.

[12] M. Moulick, S. Kumar, Comparative stress analysis of elliptical and cylindrical pressure vessel with and without Autofrettage consideration using finite element method, *International Journal of Advanced Engineering Research and Studies*, (2015) E-ISSN2249–8974.

[13] E. P. Popov, T. A. Balan, *Engineering Mechanics of Solids*, Pearson Education Inc. (2004).

[14] M. L. Wilkins, Use of artificial viscosity in multi-dimensional fluid dynamic calculations, *Journal of Computational Physics* 36 (1980) 281-303.

[15] T. Kalali, S. Hadidi-Moud, A Semi-analytical Approach to Elastic-plastic Stress Analysis of FGM Pressure Vessels, *Journal of Solid Mechanics* 5 (2013) 63-73.

[16] D. Benson, Computational methods in Lagrangian and Eulerian hydrocodes, *Computer Methods in Applied Mechanics and Engineering* 19 (1992) 235-394.

[17] S. P. Timoshenko, J. N. Goodier, *Theory of Elasticity*, MacGraw-Hill, New York, (2010).

[18] M. L. Wilkins, J. E. Reaugh, Plasticity Under Combied Stress Loading, *American Society of Mechanical Engineers Publication*, (1980) 80-C2/PVP-106.

[19] E. J. Caramana, M. J. Shashko, Elimination of artificial grid distortion and hourglass-type motion by means of lagrangian subzonal masses and pressure, *Journal of Computational Physics* 142 (1998) 521-561.

[20] O. R. Abdelsalam, R. Sedaghati, Design Optimization of Compound Cylinders Subjected to Autofrettage and Shrink-Fitting Processes, *Pressure Vessel Technology* 135 (2013) 1-11.

[21] ABAQUS 6.14 user manual. Dassault Systemes (2014).

محاسبه تنش پسماند ناشی از اتوفریتاژ تکی و دوگانه در سیلندر جدار ضخیم از مواد مدرج تابعی تحت بارگذاری دینامیکی

سید حسین رضی موسوی[1]، مجتبی محزون[2] ، محمد حسن کدیور[2]

[1]دانشکده مهندسی مکانیک، دانشگاه شیراز، شیراز، ایران.

[2]دانشکده مهندسی مکانیک، دانشگاه شیراز، شیراز، ایران.

چکیده: در این مقاله روشی عددی برای تحلیل دینامیکی پروسه اتوفریتاژ تکی و دوگانه در سیلندر جدار ضخیم ساخته شده از مواد مدرج تابعی تحت بارگذاری گذرا استخراج شده است. معادلات دینامیکی استخراج شده به صورت فرمول بندی صریح لاگرانژی ارائه شده است. حل گذرای صریح لاگرانژی روی نواحی شبکه‌بندی شده انجام می‌گیرد و نتایج توزیع تنش و کرنش برای مسائل مورد نظر تحت بارگذاری داخلی و خارجی حاصل می‌گردد. نتایج دینامیکی به خصوص در شرایط بارگذاری گذرا تفاوتهایی را در قیاس با حل استاتیکی نشان می‌دهد که به دلیل برهم کنش امواج تنش در تحلیل دینامیکی می‌باشد. در اتوفریتاژ دو گانه علاوه بر افزایش تنش پسماند فشاری در شعاع درونی باعث کاهش تنش کششی در شعاع خارجی نیز می‌گردد. برای مواد مدرج تابعی که خواص مواد به صورت پیوسته در راستای ضخامت سیلندر تغییر می‌کند، نتایج دینامیکی به دلیل تغییر امپدانس اکوستیکی و برهم کنش امواج تنش متفاوت از تحلیل استاتیکی می‌باشد. بی‌بعدسازی در تحلیل دینامیکی در راستای شعاع برخلاف تحلیلهای استاتیکی تابع پارامترهای دینامیکی بوده و براساس تغییر اندازه هندسی پاسخهای متفاوتی را آشکار می‌سازد. تنش پسماند ناشی از اتوفریتاژ تکی و دوگانه با اعمال فشار خارجی و سپس اعمال فشار داخلی در سیلندر ساخته شده از مواد مدرج تابعی برای بارگذاریها و متغیرهای متفاوت مواد مدرج تابعی به صورت گذرا مورد تحلیل قرار گرفته است. تنش پسماند ناشی از اتوفریتاژ دوگانه تحت بارگذاری مناسب باعث افزایش ظرفیت باربری سازه می‌گردد.

واژه های کلیدی: سیلندر ساخته شده از مواد مدرج تابعی، اتوفریتاژ دوگانه، مدلسازی دینامیکی، بارگذاری زمانمند، تنش پسماند.